frontiers in Pharmacology

ORIGINAL RESEARCH
published: 28 September 2021
doi: 10.3389/fphar.2021.738260

An Advanced Automated Patch Clamp Protocol Design to Investigate Drug—Ion Channel Binding Dynamics

Peter Lukacs[1], *Krisztina Pesti*[2,3], *Mátyás C. Földi*[1,2], *Katalin Zboray*[1], *Adam V. Toth*[1,2], *Gábor Papp*[4] *and Arpad Mike*[1,2]*

[1]Plant Protection Institute, Centre for Agricultural Research, Martonvásár, Hungary, [2]Department of Biochemistry, ELTE Eötvös Loránd University, Budapest, Hungary, [3]School of Ph.D. Studies, Semmelweis University, Budapest, Hungary, [4]Institute for Physics, ELTE Eötvös Loránd University, Budapest, Hungary

Standard high throughput screening projects using automated patch-clamp instruments often fail to grasp essential details of the mechanism of action, such as binding/unbinding dynamics and modulation of gating. In this study, we aim to demonstrate that depth of analysis can be combined with acceptable throughput on such instruments. Using the microfluidics-based automated patch clamp, IonFlux Mercury, we developed a method for a rapid assessment of the mechanism of action of sodium channel inhibitors, including their state-dependent association and dissociation kinetics. The method is based on a complex voltage protocol, which is repeated at 1 Hz. Using this time resolution we could monitor the onset and offset of both channel block and modulation of gating upon drug perfusion and washout. Our results show that the onset and the offset of drug effects are complex processes, involving several steps, which may occur on different time scales. We could identify distinct sub-processes on the millisecond time scale, as well as on the second time scale. Automated analysis of the results allows collection of detailed information regarding the mechanism of action of individual compounds, which may help the assessment of therapeutic potential for hyperexcitability-related disorders, such as epilepsies, pain syndromes, neuromuscular disorders, or neurodegenerative diseases.

Keywords: automated patch-clamp, sodium channel inhibitor, binding kinetics, epilepsy, pain, neuromuscular disorders, lidocaine, riluzole

OPEN ACCESS

Edited by:
Sarel Francois Malan, University of the Western Cape, South Africa

Reviewed by:
Clemens Möller, Hochschule Albstadt-Sigmaringen, Germany
Timm Danker, University of Tübingen, Germany

***Correspondence:**
Arpad Mike
arpadmike1@gmail.com

Specialty section:
This article was submitted to Pharmacology of Ion Channels and Channelopathies, a section of the journal Frontiers in Pharmacology

Received: *08 July 2021*
Accepted: *13 September 2021*
Published: *28 September 2021*

Citation:
Lukacs P, Pesti K, Földi MC, Zboray K, Toth AV, Papp G and Mike A (2021) An Advanced Automated Patch Clamp Protocol Design to Investigate Drug—Ion Channel Binding Dynamics. Front. Pharmacol. 12:738260. doi: 10.3389/fphar.2021.738260

INTRODUCTION

Most small-molecule sodium channel inhibitors bind to the local anesthetic binding site, and they are strongly state-dependent, showing ~10-fold–1,000-fold higher affinity to inactivated channels (Lenkey et al., 2011). For this reason, as it has long been recognized, determining an IC_{50} value with a single voltage protocol means practically nothing. Radically different IC_{50} values can be measured at different holding potentials (as an example, a roughly hundredfold difference was found in the case of fluoxetine (Lenkey et al., 2006)), and a shift of the steady-state availability curve caused by drug binding is a common phenomenon. These two phenomena are not only related, but they both are manifestations of state-dependent affinity. Determining concentration-response curves at

Abbreviations: E_{rel}, relative error; *%RMSE*, percentage root mean square error; **RFI**, "recovery from inactivation" protocol; **SDO**, "state-dependent onset" protocol; **SSI**, "steady-state inactivation" protocol.

different holding potentials, and determining the shift of steady-state availability curves at different drug concentrations are essentially equivalent experiments, as it has been discussed before—see Figure 1 of Lenkey et al. (2011). It is a general practice, therefore, that instead of a single IC_{50} value, the resting-state-, and inactivated-state-affinities (K_R and K_I) are given for individual compounds. Once K_R and K_I are known, the potency at any membrane potential can be estimated. Excitable cells, however, do not keep a constant membrane potential, but fire action potentials regularly. Whenever an action potential is fired, sodium channels undergo a series of conformational transitions, and sodium channel inhibitors dynamically associate and dissociate depending on the actual conformational distribution of the channel population. The final effect of the inhibitor will depend on how the firing rate (the temporal pattern of the membrane potential) and binding/unbinding kinetics relate to each other. This is the basis of the well-known difference between subclasses of class I antiarrhythmics, but binding/unbinding kinetics is equally important in the therapy of hyperexcitability-related skeletal muscle disorders (Simkin, 2011; Cannon, 2018), as well as diseases of the peripheral and central nervous system, such as certain pain syndromes and epilepsies. When assessing the onset/offset kinetics of a sodium channel inhibitor, one must consider the special position of the local anesthetic binding site: it is located within the central cavity of the channel, accessible only through the lipid membrane. The onset/offset process, therefore, cannot be simplified into a single-step binding/unbinding reaction (Vauquelin, 2016). The onset is often not diffusion-limited, but hindered by other possible rate-limiting steps: deprotonation of charged nitrogens (evidenced by the pH-dependence of onset rates (Lazar et al., 2015)), partitioning into the membrane (evidenced by the correlation between lipophilicity and potency (Lenkey et al., 2010; Lenkey et al., 2011)), access to the central cavity through the fenestrations and the activation gate (these open up only at depolarized conformations (Yan et al., 2017)), and formation of the high-affinity binding site (the whole binding pocket is thought to be rearranged at depolarized conformations). Rate limiting steps during offset may include delayed conformational rearrangement of the protein, unbinding, egress from the central cavity, and partitioning of the drug molecule into the extracellular aqueous phase. The last process may be further delayed if the compound has accumulated within intracellular lipid compartments, the depletion of which might require a longer time.

The development of the automated patch-clamp technique has made it possible to directly test the effect of multiple compounds on ion channels. However, in the case of sodium channel inhibitors, determination of an IC_{50} value, or even K_R and K_I values will not predict the therapeutic potential of specific compounds. One should achieve a comprehensive characterization of the mechanism of action for each compound. This, however, usually requires several months of experiments and analysis in a conventional manual patch clamp lab. Our aim was to design a method that could give us a detailed picture of the processes involved in the mechanism of action for individual compounds, without increasing the required time or the cost of measurements. We attempted to reconcile high throughput screening with detailed analysis of the mechanism of action, by maximizing useful information obtained during a rapid test of the compounds.

MATERIALS AND METHODS

Cell Culture and Expression of Recombinant Sodium Channels

The recombinant rNaV1.4 channel-expressing cell line was generated as described before (Lukacs et al., 2018) by transfection of rNaV1.4 BAC DNA constructs into HEK 293 cells (ATCC CRL-1573, RRID:CVCL_0045) by Fugene HD (Promega, Fitchburg, WI, United States) transfection reagent according to the manufacturer's recommendations. Cell clones with stable vector DNA integration were selected by the addition of Geneticin (Life Technologies, Carlsbad, CA, United States) antibiotic to the culture media (400 mg/ml) for 14 days. HEK293 cells were maintained in Dulbecco's Modified Eagle Medium, high glucose supplemented with 10% v/v fetal bovine serum, 100 U/ml of penicillin/streptomycin, and 0.4 mg/ml Geneticin (Life Technologies, Carlsbad, CA, United States). T175 – T25 For experiments cells were plated onto T25 (for Port-a-Patch experiments) or T175 (for IonFlux experiments) flasks, and cultured for 24–36 h. Before experiments cells were dissociated from the dish with Accutase (Corning), shaken in serum-free medium for 60 min at room temperature, then centrifuged, and resuspended into the extracellular solution to a concentration of 5×10^6 cells/ml.

Automated Patch Clamp Electrophysiology

Ensemble voltage-clamp recordings were performed on an IonFlux Mercury instrument (Fluxion Biosciences, Alameda CA, United States). Cell suspension, intracellular solution, and drug-containing extracellular solution were pipetted into the 384-well IonFlux microfluidic ensemble plates. Ensemble plates, in contrast to single-cell plates, contain not one but 20 holes in each cell trap, and current recording is done from 20 cells simultaneously. While this arrangement provides a higher success rate, seal resistances or series resistances cannot be measured for individual cells (for example if the seal resistance for the ensemble is 10 MOhm, it may mean that all 20 cells have an equal seal resistance of 200 MOhm, but may also mean that 19 of the cells have seals in the GOhm range, while one hole missed its cell, and thus its resistance remained ~10 MOhm). Because of this uncertainty, we performed quality control experiments, repeating some of the experiments under single-cell, gigaohm seal conditions, and compared the results (see below). Plates are divided into four "zones," typically each zone was used for a separate experiment (one particular set of compounds on one particular cell line). Each zone consists of eight separate sections, which are distinct functional units, containing one well for the cell suspension, one well for the waste, two cell "traps" (intracellular solution-filled wells under negative pressure to establish high resistance seals and then whole-cell configuration), and eight compound wells. The composition of solutions (in mM) was:

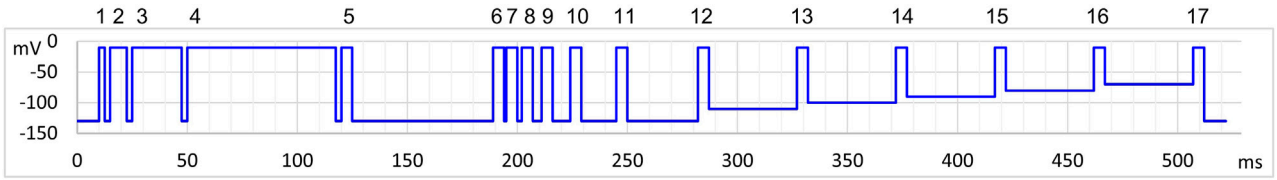

FIGURE 1 | Schematic picture of the voltage protocol. Pulses are numbered for reference.

Intracellular solution: 50 CsCl, 10 NaCl, 60 CsF, 20 EGTA, 10 HEPES; pH 7.2 (adjusted with 1 M CsOH). Extracellular solution: 140 NaCl, 4 KCl, 1 $MgCl_2$, 2 $CaCl_2$, 5 D-Glucose and 10 HEPES; pH 7.4 (adjusted with 1 M NaOH). The osmolality of intra- and extracellular solutions was set to ~320 and ~330 mOsm, respectively. All solutions were filtered with a 0.22 µm syringe filter right before the experiment. In the design of voltage protocols, the calculated 8.1 mV junction potential was taken into account. Data were sampled at 20 kHz, and filtered at 10 kHz. Experiments were carried out at room temperature. Cell ensembles were excluded if 1) the control sodium current amplitude was less than 2 nA, 2) the overall seal resistance of the cell ensemble was less than 5 MOhm, 3) a larger than 20% gradual loss of seal resistance was observed during the experiment, 4) a sudden drop of amplitude with a concurrent drop of seal resistance was observed (indicating loss of one of the cells from the ensemble). From the remaining cell ensembles of each zone, six cell ensembles were chosen for quantitative analysis, based on the stability of seal resistances. Mean seal resistances were 8.75 ± 0.30 MOhm, peak current amplitudes were 9.54 ± 0.51 nA (calculated for six-six chosen cell ensembles from 10 randomly chosen experiments).

Single-Cell Electrophysiology

Port-a-Patch (Nanion, Munich, Germany) experiments were used to validate the automated patch-clamp protocol and experimental data. Whole-cell currents were recorded using an EPC10 plus amplifier and the PatchMaster software (HEKA Electronic, Lambrecht, Germany, RRID:SCR_000034). During cell catching, sealing and whole-cell formation, the PatchControl software (Nanion) commanded the amplifier and the pressure control unit. The resistance of borosilicate chips was between 2.0 and 3.5 MΩ. The composition of solutions was identical to the ones used in IonFlux Mercury experiments.

Rationale for the Automated Patch Clamp Voltage- and Drug Perfusion-Protocol

In excitable cells sodium channels continuously change their conformations depending on the membrane potential. On the one hand, binding and unbinding of drugs are conformation-dependent, on the other hand, drug binding alters conformational transitions (gating) of channels. These interactions produce a special dynamics of continuously changing drug potency: it does not only depend on the actual value of membrane potential, but also on its recent history. To assess both membrane potential dependence and time dependence, we used the protocol illustrated in **Figure 1**. We choose to study three aspects of membrane potential-dependent dynamics of drug potency: First, the effect of inhibitors often needs some time to develop. In the first section of the protocol (pulse #1–#5), therefore, we intended to assess how fast the effect of the drug develops upon depolarization. We used progressively lengthened depolarizations and monitored the inhibition. Second, inhibitors most often dissociate from hyperpolarized (resting) channel conformation, therefore, drug potency gradually decreases upon prolonged hyperpolarization. In the second section of the protocol (pulses #6–#12) we assessed the dynamics of this recovery using progressively lengthened hyperpolarizations. Third, we assessed quasi-equilibrium conditions: we investigated in this section (pulses #13–#17) how the extent of inhibition depended on the membrane potential. The three sections of the protocol correspond with the protocols "state-dependent onset" (**SDO**), "recovery from inactivation" (**RFI**), and "steady-state inactivation" (**SSI**) we used in previous studies (Lukacs et al., 2018; Földi et al., 2021), although with some significant differences. Our priority with this current protocol was high time resolution.

For this reason, the duration of the whole 17-pulse protocol was only 522 ms, and it was repeated every second throughout the experiment. A standard experiment included seven different drug applications, 40 s long each, with 60 or 80 s wash periods between them, then the whole sequence was repeated. This means that the experiment lasted for 28–30 min, during which ~1,700–1,800 sweeps were recorded.

The microfluidic plate used in experiments contains eight compound wells, thus it would allow perfusion of eight different compounds. However, we found that solution exchange was faster and more reliable if we used compound well #1 to perfuse control extracellular solution throughout the experiment.

In the **SDO** section of the protocol (pulses #1–#5), we tested the effect of four depolarization durations (besides the control): 2.5, 7.5, 22.5, and 67.5 ms. We used a cumulative arrangement, not allowing full recovery between depolarizations (only 2.5 ms at hyperpolarized potential between depolarizations). We used Port-a-Patch experiments (i.e., in gigaseal, single-cell recordings) to verify the effects observed in IonFlux experiments (i.e., in multi-cell recordings with varying seal resistance); and also to compare the effect of this cumulative arrangement of the protocol with the conventional multi-sweep protocol, where all sweeps are started with the whole channel population in resting state. Protocols similar to this one are often used to study slow inactivation. It is important to note that in our experiments the **SDO** protocol was not intended for the study of

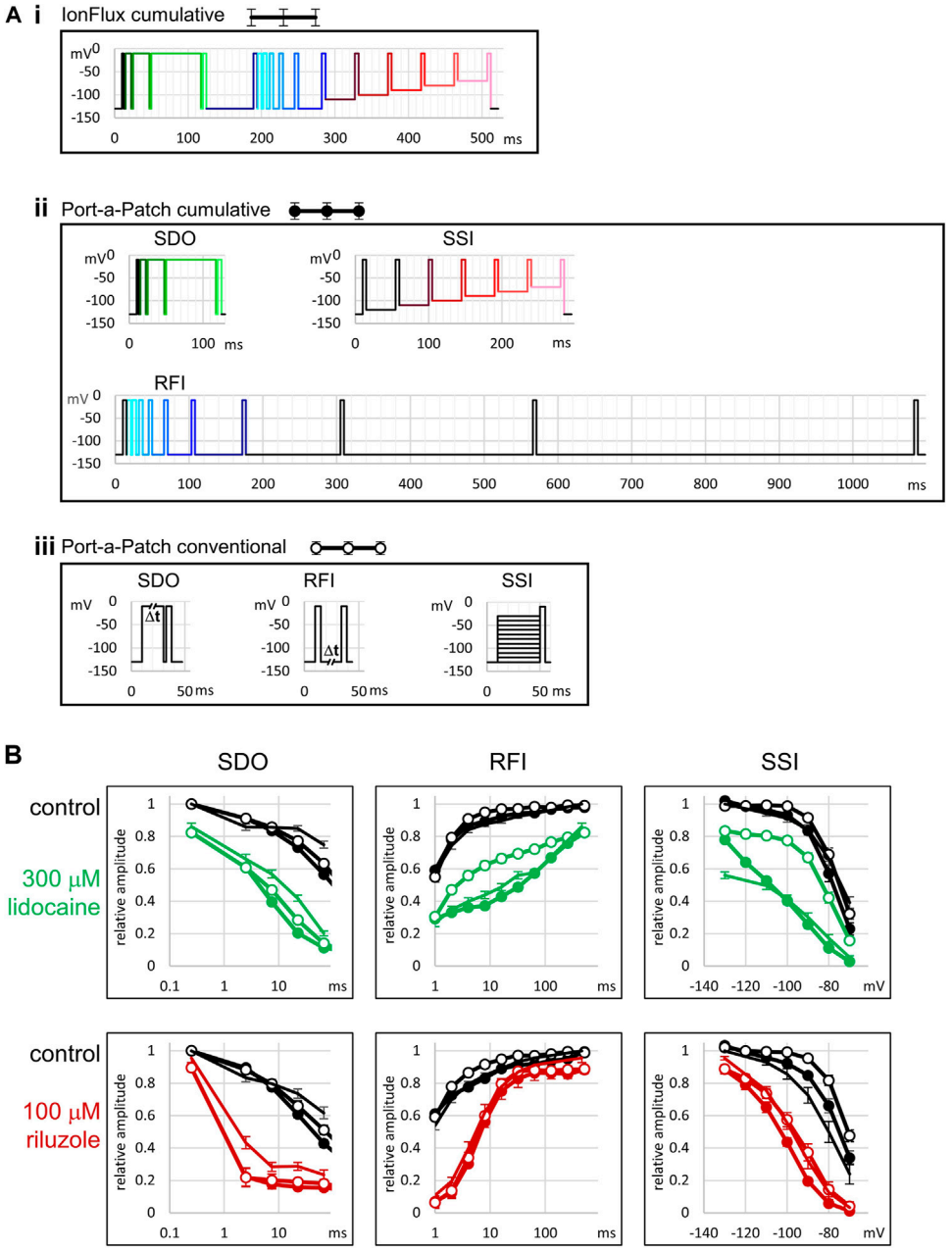

FIGURE 2 | Comparison with single-cell electrophysiology, and with conventional protocols. **(A)** Illustration of the voltage protocols under three different experimental conditions. **(i)** The 17-pulse cumulative protocol used in IonFlux experiments, as described in **Figures 1**, **3**. **(ii)** The three cumulative protocols used in Port-a-Patch experiments. Colors of pulses indicate corresponding pulses in the IonFlux protocol. The SDO protocol was exactly the same as in the IonFlux protocol The SSI section contained an extra 40 ms interpulse interval at −120 mV. The interpulse intervals of the RFI section were: 1, 2, 4, 8, 16, 32, 64, 128, 256, and 512 ms. In contrast, the interpulse intervals in the IonFlux protocol were: 1, 2, 4, 8, 16, 32, 64 ms (preceding the shorter intervals), and 498 ms (time between sweeps). **(iii)** The three conventional protocols used in Port-a-Patch experiments. **(B)** Results obtained by the protocols. This series of experiments was designed to address two questions: Are there differences between results obtained using ensemble recordings (IonFlux—lines with no circles) and single-cell recordings (Port-a-Patch—lines with closed circles)? Are there differences between results obtained using cumulative (Port-a-Patch—lines with closed circles) and conventional (Port-a-Patch—lines with open circles) protocols? Black color indicates control in all figures; Green—300 μM lidocaine; Red—100 μM riluzole.

slow inactivation, but the study of drug effect onset, upon depolarization-induced conformational change. Depolarized conformations (open and inactivated) provide increased affinity, and/or increased accessibility to the binding site, thereby allowing the development of a new binding/unbinding equilibrium. The protocol investigates how fast this new equilibrium is reached. Slow inactivation may only play a minor role in the development of the effect, since even the

longest duration (64 ms) is insufficient to induce substantial slow inactivation. The interpulse interval (2.5 ms) was chosen so that it would not allow full recovery even from fast inactivation. This way we maximized sensitivity to drug effects: if any drug stayed bound for at least 2.5 ms then it produced either channel block or delayed recovery by modulation; in both cases, the effect was sure to be detected. Thus far we have encountered only one single compound that could fully dissociate within 2.5 ms, and thus its effect was undetected in the **SDO** protocol (see the accompanying paper (Pesti et al., 2021)). In order to assess the reliability and quality of measurements in the IonFlux Mercury instrument, we performed similar experiments using the Port-a-Patch instrument. The first question was, whether the results obtained by ensemble recording reliably reproduce data measured in single-cell, gigaseal recording. The second question was, whether cumulative protocols are as informative and as sensitive as conventional protocols. The protocols used in the Port-a-Patch experiments are shown in **Figure 2A**. The comparison in the case of **SDO** protocols (**Figure 2B**, **SDO**) showed that the overall patterns were reproduced, although the effect of prolonged depolarizations was somewhat compromised in IonFlux experiments, resulting in slightly less inhibition both in control and in the presence of inhibitor drugs. This may be due to the imperfect voltage control, when some of the cells in an ensemble are imperfectly sealed. The difference between the conventional multi-sweep protocol, and the cumulative protocol (both measured under single-cell conditions), however, was negligible.

In the case of the **RFI** protocol, we used 8 hyperpolarization durations: 1, 2, 4, 8, 16, 32, 64, and 498 ms. The 64 ms hyperpolarization also served to separate the **SDO** and **RFI** sections of the protocol (to allow time for recovery). In the case of slowly acting drugs, where state-dependent binding equilibrium was not reached within 64 ms, we occasionally observed non-monotonous recovery (see the legend of **Supplementary Figure S1** for discussion). The longest (498 ms) hyperpolarization was not recorded (except its first 10 ms after the last pulse and its last 10 ms before the first pulse of the next sweep). In **Figure 2B** (**RFI**), we can observe, that results obtained with the cumulative protocol were practically identical in ensemble recordings (IonFlux) and single-cell recordings (Port-a-Patch). The conventional protocol allowed a slightly faster recovery in control, while in the presence of inhibitor drugs there was either a definite difference (300 μM lidocaine) or no significant difference (100 μM riluzole), depending on the properties of the drug (see below). The higher sensitivity of the protocol to the effects of certain drugs does not make it irrelevant regarding *in vivo* effects, in fact, the prolonged inter-sweep hyperpolarizations of the conventional protocol are non-physiological, and the pattern of the cumulative protocol resembles high-frequency trains of action potentials more closely.

Instead of a conventional **SSI** protocol, where full recovery to resting state is allowed between sweeps of the protocol, we used an accelerated procedure to assess membrane potential dependence, which did not include hyperpolarizations. This means, that resting/inactivated equilibrium was approached from a fully inactivated channel population, not from a fully resting population. If there was a true steady-state, this would make no difference. We used 40 ms pre-pulse duration, which allowed ~90% recovery from fast inactivation at −130 mV membrane potential, and somewhat less at less negative potentials. Consequently, this "no-hyperpolarization" protocol gave similar results to the conventional protocol under control conditions (see **Figure 2C**, **SSI**), although the steady-state availability curve was slightly left-shifted (by less than 5 mV). Recording from cell ensembles could cause an additional <5 mV shift, probably because of the contribution of imperfectly sealed cells. (On the one hand, the leakage itself may weaken voltage control; on the other hand, imperfectly sealed cells may themselves show left-shifted availability curves, which is a sensitive marker of cell stress (Morris and Joos, 2016)). The effect of inhibitor compounds, nevertheless, was similar to the data recorded in single-cells. The cumulative protocol was more sensitive to drug effects: it detected a larger $V_{1/2}$ shift because the effect of shifted equilibrium was accompanied by the effect of delayed recovery from inactivation. The difference was small for riluzole but much larger for lidocaine, because the extent of difference depended on drug onset/offset dynamics (see below). Although this specific protocol is admittedly a result of compromise for the sake of high temporal resolution, we believe that a series of depolarizations occurring at 22.2 Hz from membrane potentials that are close to the resting membrane potential of excitable cells is more relevant with regard to physiological effect than a protocol with prolonged <−100 mV hyperpolarizations. There was an additional practical advantage of the "no-hyperpolarization" protocol: It eliminated the problem of sub-threshold activation during pre-pulses due to poor space clamp. This is important when seal resistance and series resistance values for individual cells are poorly controlled.

Data Analysis

Using the data acquisition software, all data traces were exported in csv file format. A custom software was developed in Octave (RRID:SCR_014398) to automatically process raw data. All traces were read in from the DataAcquisition*.ISD files containing the raw data. Separate csv files contained the description of the voltage protocol. First, 2 ms sections were selected after each of the 34 voltage steps. No online (P/n) leak subtraction was employed. Capacitive artifacts were removed by calculating the sum of the section recorded at the beginning and after the end of the pulse, and then subtracting the offset so that all currents started at zero current level. Although other voltage-gated channels were present in the cells, their contribution to the fast transient inward current was small (the peak amplitude of the TTX-resistant fraction of the fast transient inward current was 5.17 ± 3.44% of the full amplitude), thus allowing reasonably accurate assessment of the extent of sodium channel inhibition. For all ~1,700 sweeps, and for all 17 pulses, the minima (peak amplitudes) were extracted and saved in 64 csv files for the 64 cell ensembles. These data (all 17 peak amplitudes for each second of a ~1,700 s experiment plotted against time) are shown for one particular cell ensemble in **Figure 3**. From each of the four zones (separate experiments), we chose n = 6 ensembles for analysis,

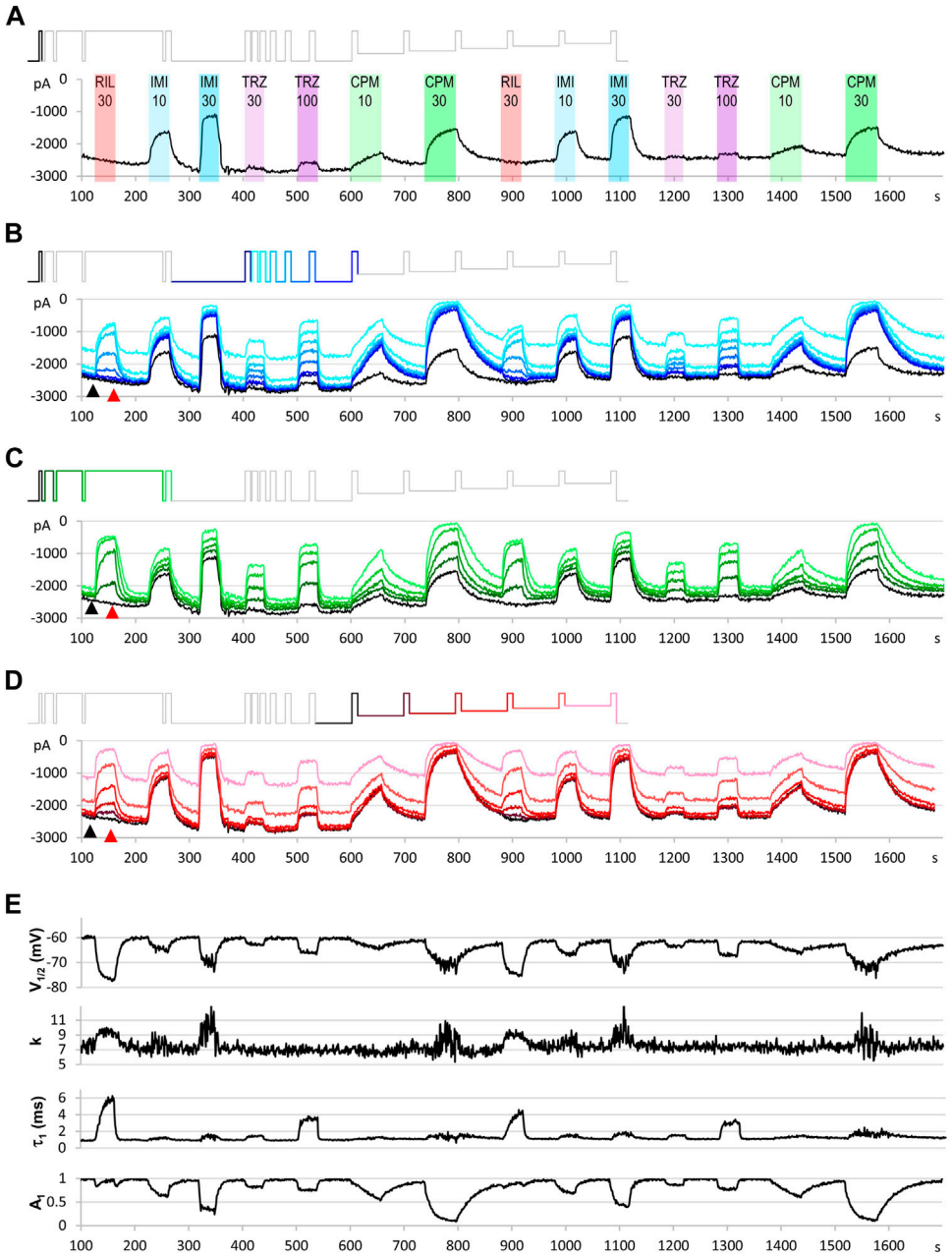

FIGURE 3 | An example for the plot of current amplitudes throughout the experiment. The experiment included two repetitions of seven different compound applications: 30 μM riluzole, 10 and 30 μM imipramine, 30 and 100 μM trazodone, 10 and 30 μM chlorpromazine. Currents evoked by all 17 depolarizations are shown, grouped into three functional assays, as described in the text. **(A)** Peak amplitude plot for pulse #1-evoked current throughout the experiment. **(B)** Currents evoked by pulses #1 and #6–#12; these allow second-to-second reconstruction of recovery from inactivation (RFI; see *Materials and Methods*) throughout the experiment. **(C)** Currents evoked by pulses #1–#5; these allow reconstruction of the **SDO** plots (see *Materials and Methods*). **(D)** Currents evoked by pulses #1 and #13–#17; these allow reconstruction of the **SSI** plots (see *Materials and Methods*). Insets show the schematic picture of the voltage protocol, where colors match the color of the corresponding amplitude plot. **(E)** Results of the automated analysis. Automated fitting of **SSI** and **RFI** data was done as described in *Materials and Methods*. The plot shows the changes in half inactivated voltage ($V_{1/2}$) and slope (k) values from **SSI** data, and the value (τ_1) and contribution (A_1) of the fast time constant from RFI data.

based on the stability of amplitude and seal resistance throughout the experiment.

SSI and **RFI** plots for each sweep were fitted by the Octave script. Fitting 64 × 1,700 plots could not be individually visually supervised, but parameters of the automated fitting were evaluated by comparing them to visually controlled fits of **SSI** and **RFI** plots, as shown in Results. At the end of all drug perfusion periods, as well as at the end of control periods before and after them, we fitted data using the Solver add-in of Microsoft Excel (RRID:SCR_016137). The precision of the

automated fit and the adequacy of the equation used were evaluated; if we found the fitting inadequate, either the equation or the constraints were modified. To evaluate the precision of the fit we calculated the root mean square error (*RMSE*) values for each fit, as well as relative error (E_{rel}) values for each point, were recorded and saved in a separate csv file. The following formulas were used to calculate the extent of error:

$$RMSE = \sqrt{\frac{1}{n}\sum_{i=1}^{n}\left(I_{exp} - I_{fit}\right)^2} \quad (1)$$

$$E_{rel} = \frac{\left|I_{exp} - I_{fit}\right|}{I_{exp}} \quad (2)$$

where n is the number of points fitted, I_{exp} is the experimentally measured amplitude, and I_{fit} is the fitted amplitude. We expressed *RMSE* values as a percentage of the maximal amplitude (for each sweep, the amplitude of the current evoked by pulse #1 of that particular sweep). The advantage of automated fitting of all **SSI** and **RFI** plots throughout the experiment was, that second-to-second changes in $V_{1/2}$, k, A_1, and τ values reveal the dynamics of development/removal of modulatory drug effect more accurately; furthermore, even minimal effects were detectable, because the tests were repeated several times before, during, and after drug applications.

Peak amplitudes of currents evoked by pulses #12–#17 were used to construct **SSI** curves, which were fit using the Boltzmann function:

$$I = I_{max} * \left(1 - \frac{1}{1 + \exp\left(\frac{V_p - V_{1/2}}{-k}\right)}\right), \quad (3)$$

where V_p is the pre-pulse potential, $V_{1/2}$ is the voltage where the curve reached its midpoint and k is the slope factor. Currents evoked by pulses #1, and #6–#12 were used to construct **RFI** plots, which were fitted with a bi-exponential function:

$$I = I_{max} * \left(A_1 * \left(1 - \exp\left(\frac{-t_{ip}}{\tau_1}\right)\right) + \left(A_2 * \left(1 - \exp\left(\frac{-t_{ip}}{\tau_2}\right)\right)\right)\right), \quad (4)$$

where τ_1 and τ_2 are the fast and slow time constants, A_1 and A_2 are their respective contribution to the amplitude, and t_{ip} is the duration of the interpulse interval. We routinely used constrains $\tau_1 < \tau_2$, and $A_1 + A_2 = 1$; and for automated fitting we also constrained the slow time constant. We found that in the presence of riluzole **Eq. 4** could not adequately fit RFI plots, therefore we used an extended equation:

$$I = I_{max} * \left(A_1 * \left(1 - \exp\left(\frac{-t_{ip}}{\tau_1}\right)^x + \left(A_2 * \left(1 - \exp\left(\frac{-t_{ip}}{\tau_2}\right)\right) + A_3\right)\right), \quad (5)$$

where A_3 represents the unmodulated fraction of channels at low riluzole concentrations which recover as control channels, and the exponent "x" was needed because recovery in the presence of riluzole has been repeatedly found to be steeper than exponential. (This has been addressed either by including a time delay parameter in the equation (Benoit and Escande, 1991; Hebert et al., 1994), or by using an equation where the fast exponential component was on the x^{th} power (Lukacs et al., 2018; Földi et al., 2021). We prefer the latter, because introducing a delay parameter results in negative numbers at short time intervals.)

We did not perform an automated fit of **SDO** plots, because fitting often required different functions for different drugs. Analysis of **SDO** data is described in the accompanying paper (Pesti et al., 2021).

The microfluidics of the IonFlux instrument could provide complete solution exchange within the 498 ms hyperpolarization (478 ms of which was unrecorded), therefore solution exchange rate did not compromise kinetic analysis of data. Complete solution exchange between sweeps was verified using high Ca^{2+} ion concentration (35 mM) containing solution (which blocks sodium channels).

In a regular experiment, only the first set of compound applications were evaluated, repetition of the experiment served as an internal control: it helped to detect incomplete recovery (see e.g. after 30 μM chlorpromazine in **Figure 3**), and to verify onset and offset rates (see e.g. the offset after 30 μM imipramine, where some disturbance obscured the offset process). It also helped to assess the extent of the spontaneous leftward shift of the steady-state availability curve by observing the ratio of the 17th/12th pulse evoked current amplitudes (pink and darkest red traces in **Figure 3D**).

RESULTS

Initial Examination of Data

In order to better explain how to interpret our data, we will first show an example for a single experiment, and make a few important general observations. After explaining the interpretation of results, we will describe how quantitative analysis from multiple experiments with multiple concentrations is performed, on the example of lidocaine and riluzole.

Figure 2 illustrates the results of a single experiment. In this example, we perfused the following compounds: riluzole (30 μM), imipramine (10 and 30 μM), trazodone (30 and 100 μM), and chlorpromazine (10 and 30 μM). The full voltage protocol (**Figure 1**) is described in the Methods section, in the interest of clarity here we will discuss it as if it was built up step-by-step.

Let us first consider what would happen if we gave only single depolarizing pulses at every second (**Figure 3A**). The peak amplitude plot shows that the amplitude was fairly stable throughout the ~30-min experiment. Riluzole at 30 μM caused no inhibition whatsoever, trazodone inhibited peak amplitudes only minimally (~5% inhibition at 100 μM), the other two compounds caused concentration-dependent inhibition. Imipramine seemed to be the most potent compound, causing ~50–55% inhibition at 30 μM.

Let us now consider the section of the experiment in which we tested the rate of recovery from inactivation (**RFI**). Current amplitudes evoked by the highlighted part of the voltage protocol are plotted throughout the experiment in **Figure 3B**. Colors in the voltage protocol match colors in the current amplitude plot. We applied consecutive depolarizing pulses with increasing interpulse intervals between them within a

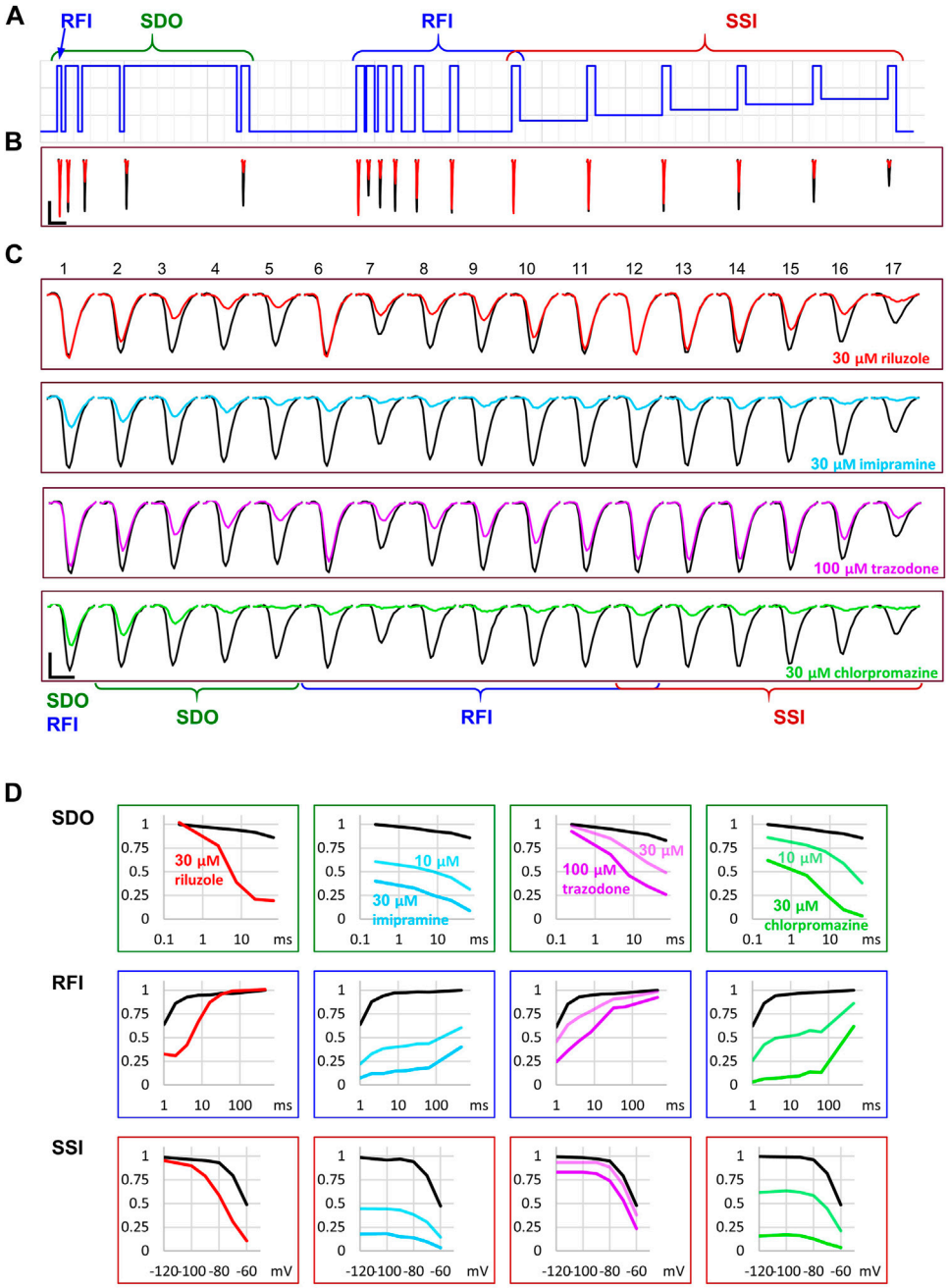

FIGURE 4 | Reconstruction of SDO, RFI, and SSI plots from the current amplitude plots. **(A)** The voltage protocol (for reference). **(B)** Evoked currents in control, and in the presence of 30 µM riluzole, shown on the same time scale as the scheme of the protocol. Note the difference in the potency of riluzole between subsequent depolarizations. Scale bars: 1 nA, 10 ms. **(C)** Evoked currents on an expanded time scale for visibility, before, and during the perfusion of riluzole, imipramine, trazodone, and chlorpromazine. Scale bars: 1 nA, 1 ms. **(D)** Reconstruction of **SDO**, **RFI**, and **SSI** plots before, and during the perfusion of the indicated compounds.

single sweep (i.e., within a single uninterrupted period of data acquisition). Interpulse intervals were 1, 2, 4, 8, 16, 32, 64, and 498 ms (not in this sequence, see colors in the protocol, as described in more details in Methods). Peak amplitudes evoked after 1 ms hyperpolarization are shown as a light blue line, currents evoked after progressively longer interpulse intervals are shown by increasingly darker shades of blue. The black line indicates the current evoked after 498 ms hyperpolarization, it is identical to the one shown in **Figure 3A**. We can observe that, in contrast to what we saw in **Figure 3A**, riluzole (30 µM) and trazodone (100 µM) did produce a massive inhibition, only the inhibition by these compounds was transient, re-appearing and disappearing within each 1 s cycle. We can observe in the case of riluzole

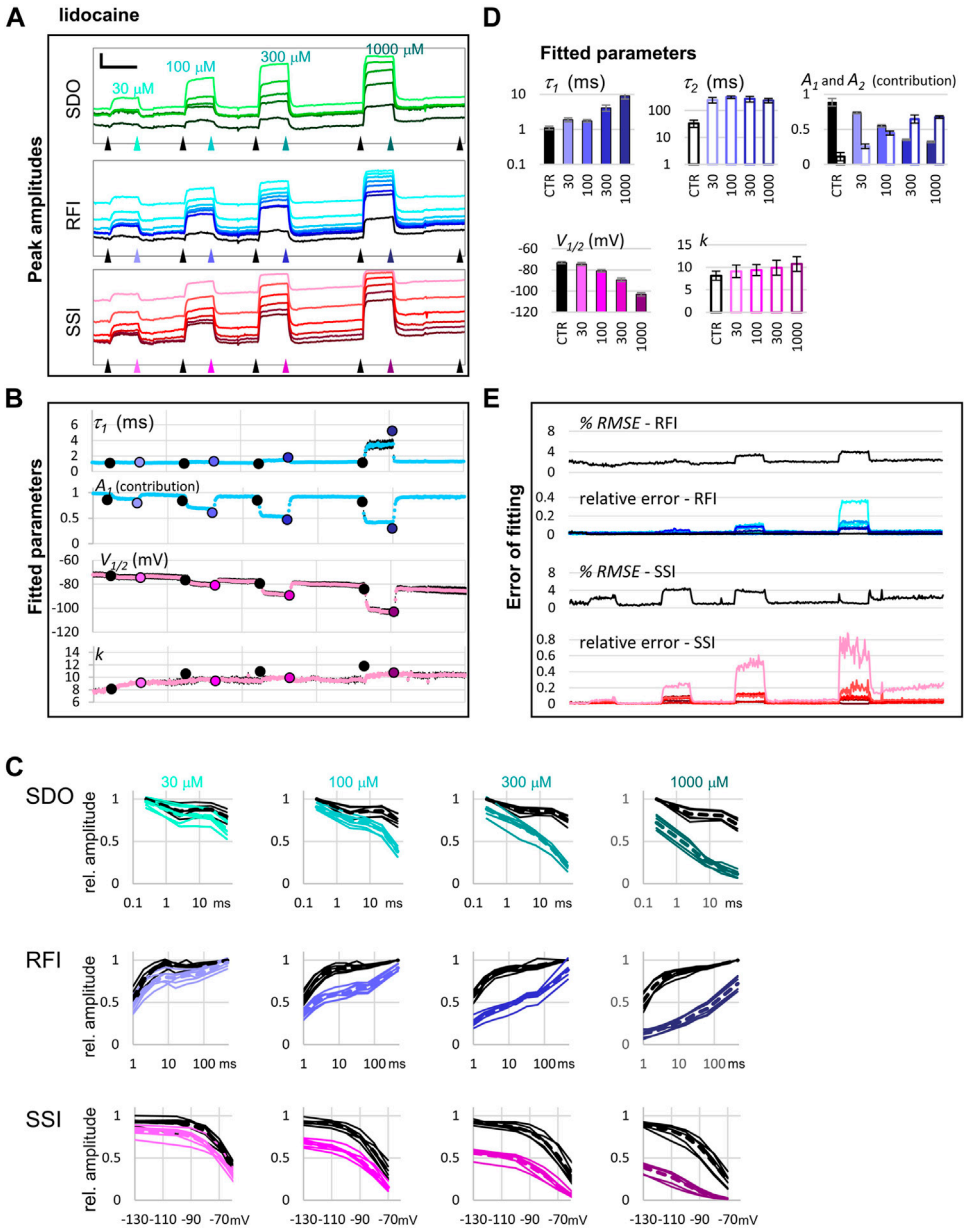

FIGURE 5 | The effect of four different concentrations of lidocaine on peak amplitudes. **(A)** An example of peak amplitude plots for all 17 pulse-evoked currents, grouped into the **SDO**, **RFI**, and **SSI** groups as shown in **Figure 2**. Scale bars: 2 nA, 50 s. Arrowheads indicate the time points immediately before, and at the end of drug perfusion periods. At each point, indicated by the arrowheads, the average of three consecutive data points was taken to construct the plots shown in panel **(C)**. **(B)** Parameters of Boltzmann, and bi-exponential automated fits throughout the four drug application periods. Colored circles indicate the values obtained by visually controlled fitting of $n = 6$ curves; the same data that is shown in panel **(C)**. **(C)** Reconstructed **SDO**, **RFI**, and **SSI** plots for $n = 6$ cell ensembles. Colors match the colors of arrowheads in panel **(A)**. Dotted lines show the average of the six cell ensembles. **(D)** Parameters obtained by visually controlled fitting of RFI and SSI plots. **(E)** The error of fitting throughout the four drug application periods. *RMSE* values are expressed as the percentage of the peak amplitude evoked by pulse #1 of the same sweep. Relative errors are shown for pulses #6–#12 and #1 (shades of blue and black, as shown in panel **(A)**), as well as for pulses #12–#17 (shades of red, as shown in panel **(A)**).

that inhibition already started to ease off at the 4 ms interpulse interval, and it almost completely disappeared by the end of the 16 ms interpulse. Inhibition by trazodone disappeared incrementally, some residual inhibition was present even at 498 ms. In contrast, inhibition by imipramine or chlorpromazine recovered minimally within 64 ms, substantial recovery only occurred during the longest (498 ms) interpulse interval. Note that two fundamentally different processes can be observed in **Figure 3B**: One can discern a dynamics of onset and recovery within individual sweeps, on a millisecond time scale (see **Figure 4**, below), in the continuous presence of the drug; we will call this "micro-dynamics." The dynamics of onset

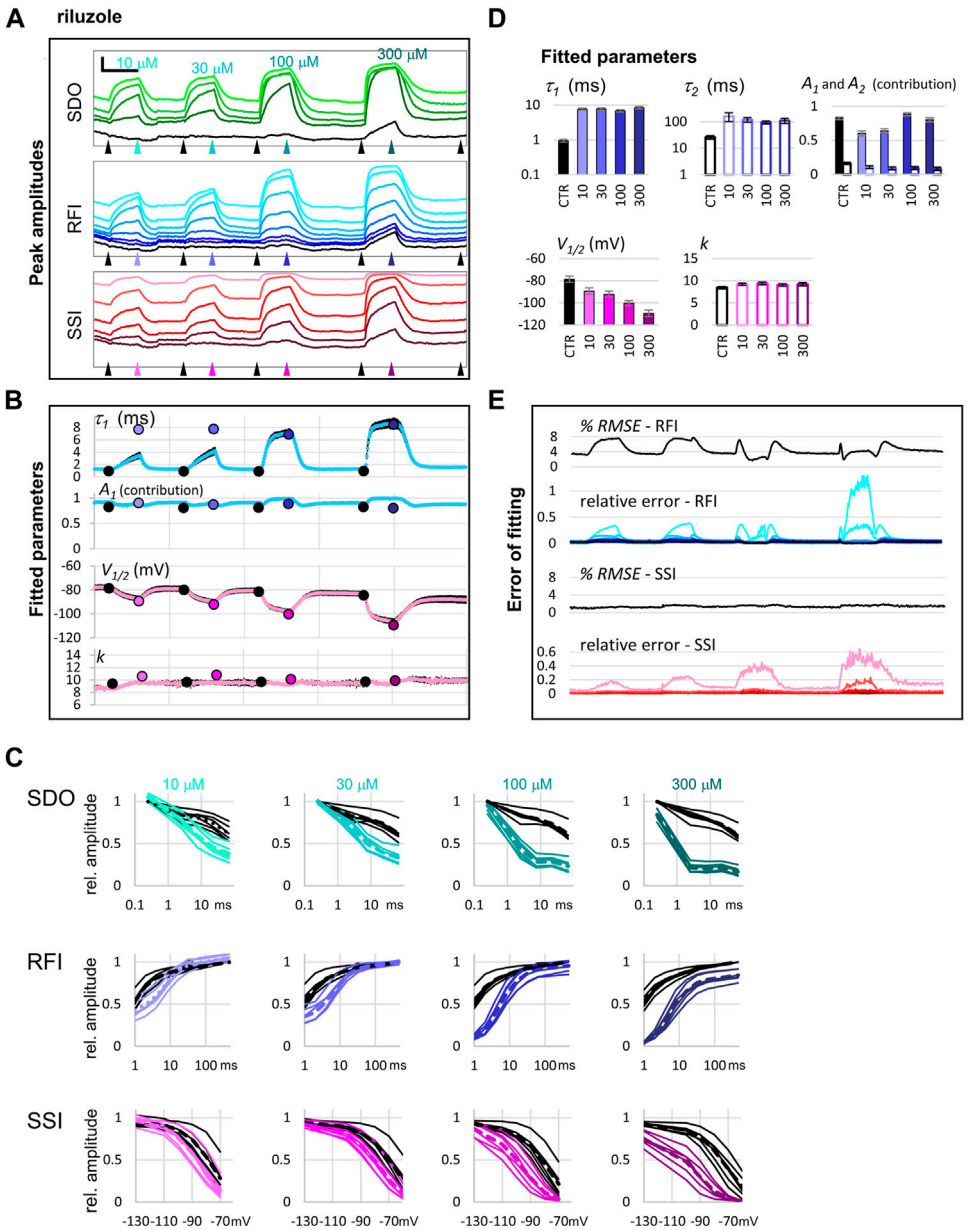

FIGURE 6 | The effect of four different concentrations of riluzole on peak amplitudes. **(A)** An example of peak amplitude plots for all 17 pulse-evoked currents, grouped into the **SDO**, **RFI**, and **SSI** groups as shown in **Figure 2**. Scale bars: 4 nA, 50 s. Arrowheads indicate the time points immediately before, and at the end of drug perfusion periods. At each point, indicated by the arrowheads, the average of three consecutive data points was taken to construct the plots shown in panel **(C)**. (B) Parameters of Boltzmann, and bi-exponential automated fits throughout the four drug application periods. Colored circles indicate the values obtained by visually controlled fitting of $n = 6$ curves; the same data that is shown in panel **(C)**. **(C)** Reconstructed **SDO**, **RFI**, and **SSI** plots for $n = 6$ cell ensembles. Colors match the colors of arrowheads in panel **(A)**. Dotted lines show the average of the six cell ensembles. **(D)** Parameters obtained by visually controlled fitting of RFI and SSI plots. For RFI plots **Eq. 5** was used, with the constraint of $x = 1$. **(E)** The error of fitting throughout the four drug application periods. *RMSE* values are expressed as the percentage of the peak amplitude evoked by pulse #1 of the same sweep. Relative errors are shown for pulses #6–#12 and #1 (shades of blue and black, as shown in panel **(A)**), as well as for pulses #12–#17 (shades of red, as shown in panel **(A)**).

and offset upon drug application and removal, on the other hand, occurred on the time scale of seconds, we will call that "macro-dynamics." Macro-dynamics provides valuable information regarding the physicochemical properties of individual compounds, which determine their *in vivo* pharmacokinetics, and the extent of their accumulation within the plasma membrane and intracellular compartments. Note, however, that it is micro-dynamics that determines firing frequency-dependent inhibition of excitable tissues. Macro-dynamics, as observed upon rapid wash-in and wash-out of drug-containing solution *in vitro*, does not occur during *in vivo* drug delivery.

Next, let us observe the section of the protocol which investigates "state-dependent onset" (**SDO**), i.e., the micro-dynamics of inhibition onset at depolarized membrane potential (**Figure 3C**). It shows currents evoked by depolarizations #1–#5, as shown by the colors of the highlighted section of the protocol. We can observe that the micro-dynamics of onset can be rather different from that of recovery, for example in the case of chlorpromazine, we see a gradual onset during the 2.5–67.5 ms depolarizations, while we can observe that most of the recovery occurred between 64 and 498 ms.

Finally, depolarizations #12–#17 assess steady-state availability at membrane potentials −130, −110, −100, −90, −80, and −70 mV (**Figure 3D**).

Parameters of the automatized fitting of **SSI** and **RFI** plots are shown in **Figure 3E**. We can observe again that different compounds behaved differently. Riluzole, which seemed to have no effect at all in **Figure 3A**, was the most potent of all drugs in terms of shifting the $V_{1/2}$ value. Trazodone was the only compound that did not affect the slope of the availability curve (k). Delayed recovery from inactivation in the case of riluzole and trazodone was predominantly due to an increase in the fast time constant, while in the case of imipramine and chlorpromazine, the fast time constant was unchanged, but its contribution was decreased. The accuracy of fits throughout the experiment can be monitored by automated calculation of $RMSE$ and E_{rel} values (**Supplementary Figure S1**).

Let us call attention to a few important points: Note that some of the inhibitors cause widely different extents of inhibition, depending on which of the 17 traces we consider. **Figure 4** illustrates micro-dynamics that took place within a single 522 ms long sweep. The voltage protocol is shown again for reference in **Figure 4A**, evoked currents are illustrated on the same time scale in **Figure 4B**, right before the first application of 30 μM riluzole (black traces), and at the end of riluzole perfusion (red traces). Black and red triangles in **Figure 2** indicate the exact time of the sweep from which original currents were taken. **Figure 4C** shows currents on an expanded time scale, we illustrate micro-dynamics during the perfusion of 30 μM riluzole (red traces), 30 μM imipramine (blue traces), 100 μM trazodone (purple traces), and 30 μM chlorpromazine (green traces). Conventional plots of **RFI**, **SDO**, and **SSI** (see *e.g.* (Lukacs et al., 2018; Földi et al., 2021)) with the four compounds are shown in **Figure 4D**.

Note also in **Figure 3**, that the observed macro-dynamics (onset time constants upon drug application and offset time constants upon washout) can also be different depending on which of the 17 pulse-evoked currents we monitor. Let us consider for example the **SDO** section of the protocol (**Figure 3C**) during the onset and offset of inhibition by 30 μM chlorpromazine. Channels activated by pulses #1 (amplitudes plotted in black) to #5 (amplitudes shown in light green) encounter the same exact concentration of the same compound during drug perfusion and subsequent washout. We know from calibration experiments that solution exchange in the extracellular aqueous phase is complete between two sweeps, however, the buildup and depletion of drug concentration within the membrane phase can be much slower, and it is the intramembrane concentration that the channel can perceive (contribution of the hydrophilic pathway is probably negligible for these strongly lipophilic compounds). The difference in potency and dynamics between traces (e.g. the light green trace and the black trace in **Figure 3C**) reflects different sensitivities of the channel, depending on its recent gating history.

If we compare the pattern produced by 100 μM trazodone and 30 μM chlorpromazine, we can observe an obvious difference not only between their macro-dynamics (both onset and offset were clearly slower for chlorpromazine) but also between their micro-dynamics. In both cases we see a gradually deepening inhibition in the **SDO** section, indicating that the onset of inhibition occurred within the investigated time window (2.5–67.5 ms). Recovery, however, was different: the effect of trazodone recovered rapidly, mostly within 64 ms (see pulse #6 in **Figure 4C**); while inhibition by chlorpromazine was not much relieved throughout the whole 17-pulse sweep, and substantial recovery only occurred during the 498 ms inter-sweep intervals.

Riluzole and trazodone showed intensive micro-dynamics: during the inter-sweep intervals, much of the inhibition was relaxed, while it was repeatedly re-established upon depolarizations. Imipramine, in contrast, showed minimal micro-dynamics, once the inhibition was established (by the end of the **SDO** section), the hyperpolarizations within the sweep (up to 64 ms) were not long enough to allow significant recovery. Even the 498 ms inter-sweep hyperpolarization was enough only for partial recovery. For this reason, **SSI** data could not be correctly measured, much longer periods would be required for establishing equilibrium. This protocol was optimized for the study of compounds with fast micro-dynamics, therefore it was inaccurate for slower micro-dynamics compounds. Chlorpromazine was similar to imipramine, with somewhat faster micro-dynamics, but slower macro-dynamics. A larger fraction of channels recovered during inter-sweep intervals, but during each sweep, after the inhibition was re-established (by the end of pulse #5), all pulses were inhibited similarly, because of the insufficient time for equilibration.

From the initial examination of this single experiment, it is apparent that different drugs have their own characteristic "signature" pattern of inhibition. This is evident from the similarity of repeated drug application effects, as well as from the effect of different concentrations of the same drug. When different concentrations of the same compound were applied, we could observe different extents of inhibition, different onset rates, but the offset rates were similar, and there was a uniform overall pattern (i.e. which of the 17 pulse-evoked currents were affected to what extent). It is clear that the voltage protocol we used could only appropriately characterize drugs with fast micro-dynamics; this protocol was intended to characterize compounds that could selectively inhibit pathological high-frequency firing. Similar protocols, with longer hyperpolarization and depolarization durations (and, therefore, necessarily with less temporal resolution) can be used for compounds with slower micro-dynamics.

In summary, initial examination indicated that these four compounds acted in four different ways. In the next section, we will show an example for an initial analysis of the effect of two well-known drugs, lidocaine, and riluzole in different concentrations. The accompanying paper (Pesti et al., 2021) will discuss how to derive compound-specific biophysical properties from this initial analysis.

Quantitative Analysis

We illustrate quantitative analysis in the case of two well-known sodium channel inhibitors, lidocaine (30, 100, 300, and 1,000 μM; **Figure 5**), and riluzole (10, 30, 100, and 300 μM; **Figure 6**). **Figures 5A**, **6A** show an example of the effect of both drugs on all 17 pulse-evoked current amplitudes. From the 17 peak amplitudes of each sweep, **SDO**, **RFI,** and **SSI** plots were reconstructed, but only **RFI** and **SSI** plots were fitted. Two different methods were used for fitting: automated fitting was performed for each sweep of the ~1,700 sweep experiment, and to validate the (uncontrolled) automated fitting, we fitted **RFI** and **SSI** plots with visual control only for pairs of control and drug-treated cell ensembles, as marked by the arrowheads in **Figures 5A**, **6A**. For all visually controlled fits three consecutive sweeps were averaged; the last three before each drug perfusion period, and the last three at the end of each drug perfusion. The **SDO**, **RFI**, and **SSI** plots, constructed from these three-point averages for six cell ensembles as well as the average of the six measurements (dashed lines)are shown in **Figures 5C**, **6C**. Light to dark color of plots (teal for **SDO**, indigo for **RFI**, and purple for **SSI** plots) indicate increasing concentration, these colors match the colors of corresponding arrowheads in **Figures 5A**, **6A**, as well as the colors of columns in **Figures 5D**, **6D**, where parameters from the visually controlled fitting are summarized. Six parameters are shown, τ_1, τ_2, A_1, and A_2 values for **RFI** fits, $V_{1/2}$, and k for **SSI** plots. In the automated fitting procedure, the slow time constant (typically between 100 and 400 ms) was fixed, because there were few data points in this time range. We calculated the mean slow time constant from the visually controlled fitting and then used this fixed value throughout the automated fitting procedure. In addition, we used the constrain of $A_1 + A_2 = 1$. For this reason, only four parameters are shown, τ_1, and A_1 values for **RFI** fits (blue dots), $V_{1/2}$, and k for **SSI** plots (pink dots) (**Figures 5B**, **6B**). For the sake of comparison, parameters obtained from the visually controlled fitting are also shown in these figures, as large circles. We can observe that the automated fitting procedure quite reliably reproduced data from the visually controlled fitting, except in the case of 10 and 30 μM of riluzole (see below for an explanation). The overall quality of the fit could be monitored by observing the % *RMSE* values; from the E_{rel} values, we could see which particular point contributes most to the error. In the case of both riluzole and lidocaine E_{rel} values were quite low, except for pulses #7, #8, and #17; where peak amplitudes were the smallest. Small amplitudes necessarily result in a higher relative error, both because of the decreased signal-to-noise ratio and because the fitting procedure minimizes absolute, not relative, squared errors.

In the **RFI** plots, lidocaine caused a slowing of the fast time constant of recovery, which was moderate at lower concentrations (30 and 100 μM) but was substantial at 300 and 1000 μM concentrations (~4-fold and ~7-fold, respectively). More importantly, the contribution of the slow time constant gradually overcame the contribution of the fast one, increasing from 8.8 ± 2.1% at control, to 68.8 ± 1.4% at 1,000 μM, while the value of the slow time constant did not change with concentration (**Figure 5D**). In contrast, riluzole caused no change in either the contribution or the value of the slow time constant but caused a radical ~8-fold increase in the fast time constant. The extent of this increase did not change significantly with concentration (ranging from 7.4- to 8.9-fold), but at lower concentrations there seemed to be an unmodulated fraction of the channel population, as it can be seen on the contribution of A_1 at concentrations 10 and 30 μM (**Figure 6D**).

In the **SSI** plots, both compounds caused a concentration-dependent hyperpolarizing shift in the half inactivation voltage, while the slopes did not change significantly.

In summary, it was possible to perform automated fitting of ~1,700 **RFI** and **SSI** plots on 64 channels, with reasonable accuracy. *RMSE* values remained below 4%, except for **RFI** plots in the presence of riluzole, where the conventional bi-exponential equation was clearly inadequate for fitting the data. In this special case recovery data have been consistently found to be steeper than exponential, and therefore either have been fit with an equation that included a time delay parameter (Benoit and Escande, 1991; Hebert et al., 1994), or with an equation where the fast exponential component was on the n^{th} power (Lukacs et al., 2018; Földi et al., 2021). Visually controlled fits confirmed the parameters of automated fitting and gave somewhat better *RMSE* values (between 0.44 and 1.56% for all **SSI** fits, and between 1.12 and 2.27% for **RFI** fits in control, and in the presence of lidocaine). In the case of **RFI** plots in the presence of riluzole, visual control allowed us to identify the source of error, and to modify the equation accordingly. Fitting the **RFI** plot with the simple bi-exponential equation gave *RMSE* values 3.54, 2.97, 1.79, and 2.76%, for 10, 30, 100, and 300 μM riluzole, respectively. To improve these, we introduced the extended equation (**Eq. 5**) in two steps: in the first step, we allowed A_3 to be different from zero. Allowing a non-zero unmodulated fraction was important in the case of 10 and 30 μM concentrations, and improved their *RMSE* values to 0.64 and 0.67, respectively, but did not change the *RMSE* values for 100 and 300 μM riluzole. The parameters obtained with this modification are shown in **Figure 5D**. In the next step, we also allowed the exponent "x" to be different from 1. This improved *RMSE* values for all four concentrations: to 0.50, 0.64, 1.04 and 1.11% for 10, 30, 100, and 300 μM riluzole, respectively. By allowing the exponent to vary, however, we lost the comparability of fast time constants, because the time constant and the exponent are interdependent, as we have discussed before (Lukacs et al., 2018). This is the reason why in **Figure 5D** we show time constants from the fit when non-zero A_3 of **Eq. 5** was allowed, but the exponent was not allowed to differ from 1.

DISCUSSION

To understand the effect of drugs on ion channels, one must study the complex kinetics of ion channel gating, the complex dynamics of drug distribution (which includes partitioning between aqueous and membrane phases, entering/exiting the central cavity, and binding/unbinding), as well as the multiple interactions between the two (which come from state-dependent access, state-dependent binding, and drug-induced modulation of gating). Sodium channels undergo a fast but extensive conformational rearrangement during gating, which radically alters the accessibility and affinity of the binding site. Individual inhibitor compounds can react differently to these changes, which may confer them with unique abilities to selectively inhibit specific activity patterns. For example, riluzole is especially effective at high-frequency firing (Desaphy et al., 2014; Földi et al., 2021), phenytoin at prolonged depolarizations (Kuo and Bean, 1994; Liu et al., 2011; Terragni et al., 2016). The significance of functional selectivity, and the importance to test the effectiveness of sodium channel inhibitors under different conditions, has been recognized before, and adapting this approach to automated patch clamp instruments has been attempted. Three-pulse and four-pulse protocols have been used to study sodium channel inhibitors in order to address different aspects of functional selectivity (Liu et al., 2011; Liu, 2014). An initial attempt to study macro- and micro-dynamics in parallel, together with the effect on gating equilibrium has been made by our group earlier (Lenkey et al., 2010). In that case, however, we only used a simple 5 Hz train, which gives very limited information on micro-dynamics. In addition, the 0.05 Hz time resolution (the trains were repeated every 20 s) was inadequate for fast-acting drugs. Our method described here is novel in two aspects: First, it is able to give a simple, but complete assessment of state-dependent onset/offset dynamics of individual compounds, as well as the assessment of their effect on the conformational equilibrium of the channel, all within a single sweep of voltage steps. Second, it is able to provide this kinetic and equilibrium information at an unprecedented time resolution (1 Hz), which allowed us to monitor the development and decline of these effects upon drug application and removal.

The first important observation that this protocol allowed us to make was the obvious existence of two completely different processes, named micro- and macro-dynamics. This emphasizes the often unappreciated complexity of the processes which underlie the onset and offset of drug effect. Macro-dynamics is often studied using single pulses delivered at a certain fixed frequency, while the compound is washed in and then washed out. Macro-onset and macro-offset time constants are commonly interpreted as reflecting association and dissociation, and therefore are used to determine the affinity of binding. However, these processes never occur *in vivo*, and most likely do not reflect purely association and dissociation (only if partitioning into the membrane and access into the central cavity are relatively unobstructed, and therefore the rate-limiting step of onset is diffusion itself).

In contrast, micro-dynamics keeps going on incessantly all the time, in all excitable cells of the organism. Micro-offset is conventionally studied using the recovery from inactivation (RFI) protocol (using different interpulse intervals in separate sweeps). This recovery is also commonly interpreted as dissociation. Therefore, it is important to point out that for many inhibitor compounds micro- and macro-dynamics differ by several orders of magnitude, therefore it is not clear whether unbinding itself contributes to one, to the other, or both. For most compounds, we suppose that macro-onset may reflect deprotonation (as evidenced by the pH dependence of macro-dynamics (Lazar et al., 2015)), accumulation within the membrane phase, and state-dependent access to the central cavity. Macro-offset may reflect state-dependent egress from the central cavity and depletion of the membrane phase (and intracellular compartments). Micro-dynamics, for most inhibitors, probably reflects genuine binding/unbinding, but may also represent modulated gating (Földi et al., 2021) or the process of access/egress (diffusion between the central cavity and the membrane phase). Micro-dynamics is always dependent on conformational states, and in turn, it also affects the distribution of conformational states (by altering the rates of transitions between them).

Interestingly, although micro-dynamics obviously cannot be slower than macro-dynamics, the two are in fact not strongly correlated. We have found compounds with fast micro-dynamics but relatively slow macro-dynamics (e.g. riluzole, with more than 1,000-fold difference between micro- and macro-dynamics rates), and also some with relatively slow micro- but fast macro-dynamics (like bupivacaine, with less than 10-fold difference).

For slow micro-dynamics compounds, we will need to prolong the experimental protocol with both longer depolarizations and hyperpolarizations. Of course, this can only be done at the expense of time resolution, but for drugs, with slow dynamics, this seems acceptable. Allowing close-to-full equilibration of micro-onset and micro-offset should not compromise macro-dynamics.

In summary, automated analysis of data obtained using a complex voltage- and drug application protocol for an automated patch clamp instrument allowed us to assess the complex dynamics of drug-ion channel interaction, and to identify multiple sub-processes that constitute the onset and offset of drug effects during and after drug perfusion. Dynamics of drug binding/unbinding, access/egress, protonation/deprotonation, as well as the extent of modulation and channel block are crucial determinants of therapeutic effectiveness. We expect that a comprehensive assessment of the mechanism of action can provide a better prediction of therapeutic potential than the assessment of resting and inactivated affinity only.

DATA AVAILABILITY STATEMENT

The raw data supporting the conclusion of this article will be made available by the authors, without undue reservation.

AUTHOR CONTRIBUTIONS

PL and AM designed research; KP, MF, and AT performed automated patch-clamp experiments; AT performed single-cell patch-clamp experiments; PL, KZ, and GP contributed to the methodology and provided resources; PL and GP provided software tools; PL, MF, KP, AT, and AM analyzed data; PL and AM wrote the manuscript, all authors have read and approved the manuscript.

FUNDING

This work was supported by the Hungarian Brain Research Program (KTIA-NAP-13–2–2014–002), and by Hungary's Economic Development, and Innovation Operative Programme (GINOP-2.3.2-15-2016-00051).

ACKNOWLEDGMENTS

The content of this paper has previously appeared online in bioRxiv: https://doi.org/10.1101/2021.07.05.451189.

SUPPLEMENTARY MATERIAL

The Supplementary Material for this article can be found online at: https://www.frontiersin.org/articles/10.3389/fphar.2021.738260/full#supplementary-material

REFERENCES

Benoit, E., and Escande, D. (1991). Riluzole Specifically Blocks Inactivated Na Channels in Myelinated Nerve Fibre. *Pflugers Arch.* 419, 603–609. doi:10.1007/bf00370302

Cannon, S. C. (2018). Sodium Channelopathies of Skeletal Muscle. *Handb. Exp. Pharmacol.* 246, 309–330. doi:10.1007/164_2017_52

Desaphy, J. F., Carbonara, R., Costanza, T., and Conte Camerino, D. (2014). Preclinical Evaluation of Marketed Sodium Channel Blockers in a Rat Model of Myotonia Discloses Promising Antimyotonic Drugs. *Exp. Neurol.* 255, 96–102. doi:10.1016/j.expneurol.2014.02.023

Földi, M. C., Pesti, K., Zboray, K., Toth, A. V., Hegedűs, T., Málnási-Csizmadia, A., et al. (2021). The Mechanism of Non-blocking Inhibition of Sodium Channels Revealed by Conformation-Selective Photolabeling. *Br. J. Pharmacol.* 178, 1200–1217. doi:10.1111/bph.15365

Hebert, T., Drapeau, P., Pradier, L., and Dunn, R. J. (1994). Block of the Rat Brain IIA Sodium Channel Alpha Subunit by the Neuroprotective Drug Riluzole. *Mol. Pharmacol.* 45, 1055–1060.

Kuo, C. C., and Bean, B. P. (1994). Slow Binding of Phenytoin to Inactivated Sodium Channels in Rat Hippocampal Neurons. *Mol. Pharmacol.* 46, 716–725.

Lazar, A., Lenkey, N., Pesti, K., Fodor, L., and Mike, A. (2015). Different pH-Sensitivity Patterns of 30 Sodium Channel Inhibitors Suggest Chemically Different Pools along the Access Pathway. *Front. Pharmacol.* 6, 210. doi:10.3389/fphar.2015.00210

Lenkey, N., Karoly, R., Epresi, N., Vizi, E., and Mike, A. (2011). Binding of Sodium Channel Inhibitors to Hyperpolarized and Depolarized Conformations of the Channel. *Neuropharmacology* 60, 191–200. doi:10.1016/j.neuropharm.2010.08.005

Lenkey, N., Karoly, R., Kiss, J. P., Szasz, B. K., Vizi, E. S., and Mike, A. (2006). The Mechanism of Activity-Dependent Sodium Channel Inhibition by the Antidepressants Fluoxetine and Desipramine. *Mol. Pharmacol.* 70, 2052–2063. doi:10.1124/mol.106.026419

Lenkey, N., Karoly, R., Lukacs, P., Vizi, E. S., Sunesen, M., Fodor, L., et al. (2010). Classification of Drugs Based on Properties of Sodium Channel Inhibition: A Comparative Automated Patch-Clamp Study. *PLoS One* 5, e15568. doi:10.1371/journal.pone.0015568

Liu, Y., Beck, E. J., and Flores, C. M. (2011). Validation of a Patch Clamp Screening Protocol that Simultaneously Measures Compound Activity in Multiple States of the Voltage-Gated Sodium Channel Nav1.2. *Assay Drug Dev. Technol.* 9, 628–634. doi:10.1089/adt.2011.0375

Liu, Y. (2014). Electrophysiological Studies of Voltage-Gated Sodium Channels Using QPatch HT, an Automated Patch-Clamp System. *Curr. Protoc. Pharmacol.* 65, 11–45. doi:10.1002/0471141755.ph1114s65

Lukacs, P., Földi, M. C., Valánszki, L., Casanova, E., Biri-Kovács, B., Nyitray, L., et al. (2018). Non-Blocking Modulation Contributes to Sodium Channel Inhibition by a Covalently Attached Photoreactive Riluzole Analog. *Sci. Rep.* 8, 8110. doi:10.1038/s41598-018-26444-y

Morris, C. E., and Joos, B. (2016). Nav Channels in Damaged Membranes. *Curr. Top. Membr.* 78, 561–597. doi:10.1016/bs.ctm.2016.06.001

Pesti, K., Földi, M. C., Zboray, K., Toth, A. V., Lukacs, P., and Mike, A. (2021). Characterization of Compound-specific, Concentration-independent Biophysical Properties of Sodium Channel Inhibitor Mechanism of Action Using Automated Patch-Clamp Electrophysiology. *Front. Pharmacol.* 12, 738460. doi:10.3389/fphar.2021.738460

Simkin, D., and Bendahhou, S. (2011). Skeletal Muscle Na Channel Disorders. *Front. Pharmacol.* 2, 63. doi:10.3389/fphar.2011.00063

Terragni, B., Scalmani, P., Colombo, E., Franceschetti, S., and Mantegazza, M. (2016). Ranolazine vs Phenytoin: Greater Effect of Ranolazine on the Transient Na(+) Current Than on the Persistent Na(+) Current in central Neurons. *Neuropharmacology* 110, 223–236. doi:10.1016/j.neuropharm.2016.06.029

Vauquelin, G. (2016). Cell Membranes... and How Long Drugs May Exert Beneficial Pharmacological Activity *In Vivo* and How Long Drugs May Exert Beneficial Pharmacological Activity *In Vivo*. *Br. J. Clin. Pharmacol.* 82, 673–682. doi:10.1111/bcp.12996

Yan, Z., Zhou, Q., Wang, L., Wu, J., Zhao, Y., Huang, G., et al. (2017). Structure of the Nav1.4-β1 Complex from Electric Eel. *Cell* 170, 470–482.e11. doi:10.1016/j.cell.2017.06.039

Conflict of Interest: The authors declare that the research was conducted in the absence of any commercial or financial relationships that could be construed as a potential conflict of interest.

Publisher's Note: All claims expressed in this article are solely those of the authors and do not necessarily represent those of their affiliated organizations, or those of the publisher, the editors and the reviewers. Any product that may be evaluated in this article, or claim that may be made by its manufacturer, is not guaranteed or endorsed by the publisher.